The Astrophysical Journal, 902:90 (9pp), 2020 October 20 https://doi.org/10.3847/1538-4357/abb60a

Evidence for and Analysis of Multiple Hidden Coronal Strands in Cross-sectional Emission Profiles: Further Results from NASA's High-resolution Solar Coronal Imager

Thomas Williams[1], Robert W. Walsh[1], Hardi Peter[2], and Amy R. Winebarger[3]
[1] Jeremiah Horrocks Institute, University of Central Lancashire, Preston, PR1 2HE, UK
[2] Max Planck Institute for Solar System Research, Justus-von-Liebig-Weg 3, D-37077, Göttingen, Germany
[3] NASA Marshall Space Flight Center, ST13, Huntsville, AL 35812, USA
Received 2020 April 6; revised 2020 September 4; accepted 2020 September 6; published 2020 October 15

Abstract

Previous work utilizing NASA's High-resolution Coronal Imager (Hi-C 2.1) 172 Å observations revealed that, even at the increased spatial scales available in the dataset, there may be evidence for coronal structures that are still not fully resolved. In this follow-up study, cross-section slices of coronal strands are taken across the Hi-C 2.1 field of view. Following previous loop-width studies, the background emission is removed to isolate the coronal strands. The resulting intensity variations are reproduced by simultaneously fitting multiple Gaussian profiles using a nonlinear least-squares curve-fitting method. In total, 183 Gaussian profiles are examined for possible structures that are hinted at in the data. The full width at half maximum is determined for each Gaussian, which are then collated and analyzed. The most frequent structural widths are ≈450–575 km with 47% of the strand widths beneath NASA's Solar Dynamics Observatory Atmospheric Imaging Assembly (AIA) resolving scale (600–1000 km). Only 17% reside beneath an AIA pixel width (435 km) with just 6% of the strands at the Hi-C 2.1 resolving scale (≈220–340 km). These results suggest that non-Gaussian shaped cross-sectional emission profiles observed by Hi-C 2.1 are the result of multiple strands along the integrated line of sight that can be resolved, rather than being the result of even finer sub-resolution elements.

Unified Astronomy Thesaurus concepts: The Sun (1693); Solar coronal loops (1485); Solar corona (1483); Solar atmosphere (1477)

1. Introduction

Observational investigations of coronal loop structure have been undertaken since the 1940s (Bray et al. 1991); however, due to insufficient spatial resolution of current and previous instrumentation, the definitive resolved widths of these fundamental structures have not been fully realized. Recent high-resolution data from NASA's Interface Region Imaging Spectrometer (IRIS; De Pontieu et al. 2014) and the High-resolution Coronal imager (Hi-C; Kobayashi et al. 2014) have led to coronal loop-width studies in unprecedented detail. For short loops whose lengths are of the scale of a granule, Peter et al. (2013) found widths $\lesssim$200 km within the Hi-C data. Similarly, Aschwanden & Peter (2017) sampled 10^5 loop-width measurements from the Hi-C field of view (FOV) with their analysis finding the most-likely width ≈550 km, arguing the possibility that Hi-C fully resolved the 193 Å loops/strands. This agrees with previous work (Peter et al. 2013) where it is proposed that at least some of the wider loops with diameters ≈1 Mm observed by NASA's Solar Dynamic Observatory Atmospheric Imaging Assembly (AIA; Lemen et al. 2012) do not appear to show what they consider to be obvious signs of substructure when compared to the coincident Hi-C dataset. Combining IRIS data with hydrodynamic simulations, Brooks et al. (2016) find transition region temperature loops with widths between 266 and 386 km, and showcase that these structures appear to be composed of singular magnetic threads.

Klimchuk (2015) investigates the widths of four EUV loops as a function of position using Hi-C and AIA data, and obtain widths of 880–1410 km with Hi-C. They also find that, while the analyzed loops have relatively constant cross section along their lengths, those measured with Hi-C are typically less than 25% narrower than their AIA counterparts. Therefore, they suggest that loops are not highly under-resolved by AIA and these results further support previous findings of measured widths along both EUV (López Fuentes & Klimchuk 2006) and soft X-ray (Klimchuk et al. 1992; Klimchuk 2000) loop structures where no significant or observable expansion from the loop base to apex is determined. This work has been developed further by Klimchuk & DeForest (2020) where, for 20 loops from the first Hi-C flight data, intensity versus width measurements tended to be uncorrelated or have a direct dependence, implying that the loop flux tube cross sections themselves are approximately circular (assuming that there is non-negligible twist along the flux tube and that the plasma emission is nearly uniform along the magnetic field).

Recently, Williams et al. (2020) investigated loops from five regions within the FOV of the latest Hi-C flight but at 172 Å wavelengths (termed Hi-C 2.1; Rachmeler et al. 2019). As with Aschwanden & Peter (2017), coronal strand widths of ≈513 km were determined for four of the five regions analyzed. The final region, which investigates low emission and low density loops, finds much narrower coronal strands of ≈388 km, placing those structures beneath the width of a single AIA pixel. The fact that these strands are above the smallest spatial scale at which Hi-C 2.1 can resolve individual structures (220–340 km; Rachmeler et al. 2019) suggests that Hi-C 2.1 may be beginning to resolve a key spatial scale of coronal loops.

Notably, and the focus for this work, Williams et al. (2020) also find example structures that may not be fully resolved within the Hi-C 2.1 data. These relate to smaller "bumps" or

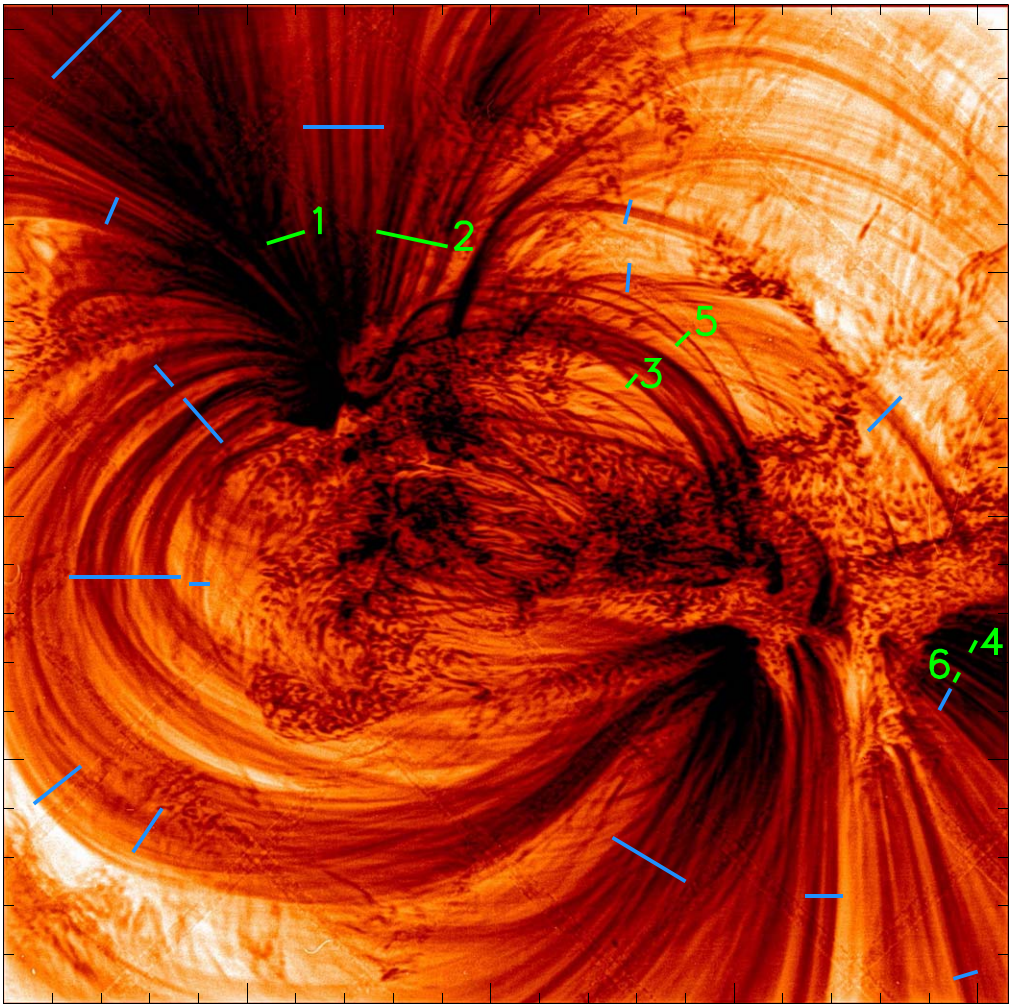

Figure 1. Reverse color image showing the Hi-C 2.1 field of view (FOV) which has been time-averaged for ≈60 s and then, for the purpose of this figure only, sharpened with Multi-Scale Gaussian Normalization (MGN; Morgan & Druckmüller 2014). The locations of the cross-section slices where multiple-peaked structures are observed are shown in blue, while the green slices are displayed more clearly in Figure 3. The cross-sectional profiles for the slices numbered 1–4 (5 and 6) are shown in Figure 5 (4).

turning points in the intensity profiles that are larger than the observational error bars but do not constitute a full, completely isolated strand. Could these be the result of projection effects of overlapping structures along the integrated line of sight for this optically thin plasma, or are they the result of further structures beneath even the resolving abilities of Hi-C 2.1?

Thus, this current paper outlines approaches to further investigate the possible spatial scale of Hi-C 2.1 coronal strands reported upon by Williams et al. (2020) but are not fully resolved as defined above. In Section 2 the Hi-C 2.1 data preparation is discussed including the Gaussian fit method employed to estimate the width of these partially resolved coronal features. The resulting distribution of fitted widths is described in Section 3 with conclusions reached on the analysis outlined in Section 4.

2. Data Preparation and Analysis Method

On 2018 May 29th at 18:54 UT, Hi-C 2.1 was successfully relaunched from the White Sands Missile Range, NM, USA, capturing high-resolution data ($2k \times 2k$ pixels; $4\farcm4 \times 4\farcm4$ FOV) of target active region AR 12712 in EUV emission of wavelength 172 Å (dominated by Fe IX emission ≈0.8 MK) with a plate scale of $0\farcs129$. During the flight Hi-C 2.1 captured 78 images with a 2 s exposure time and a 4.4 s cadence between 18:56 and 19:02 UT. Full details on the Hi-C 2.1 instrument can be found in Rachmeler et al. (2019).

2.1. Dataset Extraction and Background Subtraction

The basis of the sample dataset investigated here include a number of subsets from the ten higher-emission cross-section slices analyzed by Williams et al. (2020) plus nine other additional slices from within the Hi-C 2.1 FOV (see Figure 1 where all dataset locations are indicated). In each case the resulting emission profile across the structures would indicate substructure strands that are not fully resolved i.e., a non-Gaussian shape.

Following the method outlined in Williams et al. (2020), the Hi-C 2.1 dataset under consideration is time-averaged over a period ≈60 s that is free from spacecraft jitter.[4] Each cross section normal to each strand is taken to be 3 pixels deep and the background emission is then subtracted. As outlined in

[4] A consequence of the instability experienced during the Hi-C 2.1 flight is that ghosting of the mesh could not be avoided (Rachmeler et al. 2019). This leads to the diamond patterns across the entire Hi-C 2.1 FOV, which are exaggerated when the data is enhanced with MGN (Figure 1).

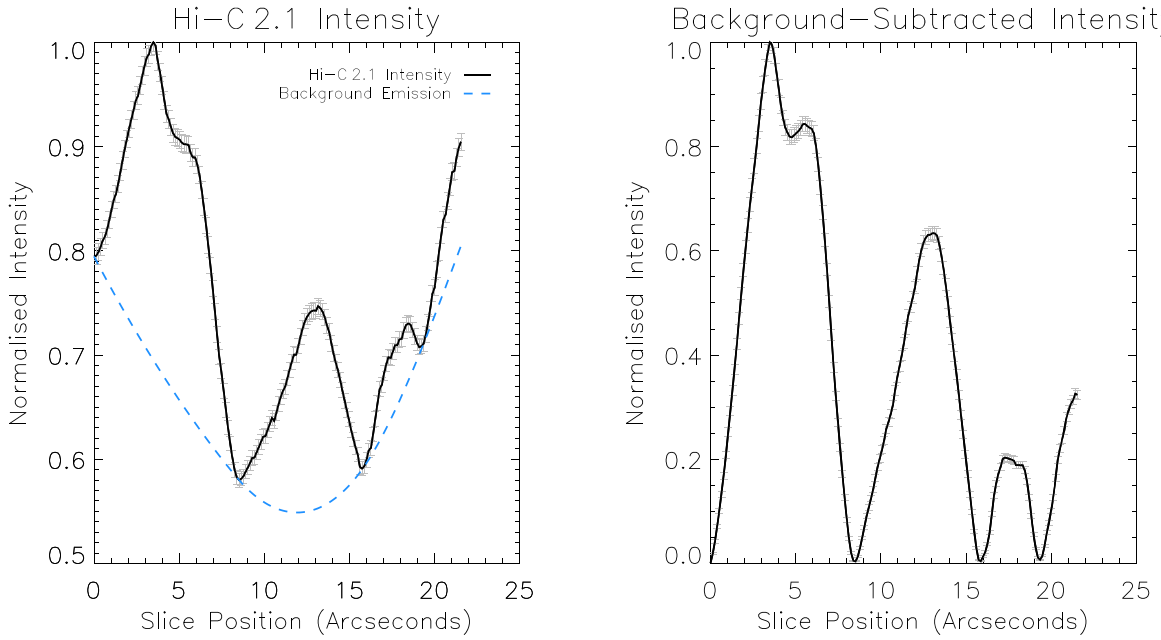

Figure 2. Left: an example cross-section slice from the Hi-C 2.1 FOV (slice 2 in Figure 1) is shown in black. The global background obtained by interpolating with a cubic spline through the inflection points is shown via the dashed blue line. Right: the isolated coronal strands that are obtained by subtracting the global background from the Hi-C 2.1 intensity. The error bars denote five times the Poisson error (gray) due to the small magnitude (mean: 1.8×10^{-3}) making them difficult to see without magnification.

Figure 2, this background subtraction is performed by first finding all the local minima of a slice, and interpolating through these values using a cubic spline (Yi et al. 2015) to obtain a global trend (dashed blue line). The global trend is then subtracted from the intensity profile along the slice, leaving behind the background-subtracted coronal strands (similar to Aschwanden & Schrijver 2011; Williams et al. 2020). Due to the large number of counts detected by Hi-C 2.1 the Poisson error associated with these isolated coronal strands is minimal (Figure 2).

2.2. Gaussian Fitting and FWHM Measurements

The analysis method is based on the assumption that at rest, an isolated coronal strand element has an observed emission profile across its width and is normal to the strand axis that is approximately Gaussian. It is important to note that, as indicated by Pontin et al. (2017), instantaneously coronal strands may not necessarily have a clear Gaussian cross section. On the other hand, Klimchuk & DeForest (2020) have shown from Hi-C observations that coronal strands are likely to have circular cross sections. To attempt to address this and as indicated previously, the data samples are time-averaged over ≈60 s (the first 11 Hi-C 2.1 frames) to average out any short timescale changes. While no obvious signs of motion within the structures analyzed are noticed in this 60 s window, the authors acknowledge that as indicated by Morton & McLaughlin (2013), small amplitude oscillations could be present, which would lead to the measured widths being broader than the structural width due to the time integration performed.

Previous width studies (such as Aschwanden & Peter 2017; Williams et al. 2020) would have considered the features under examination here (e.g., those between 0″ and 6.″5 in Figure 5) as individual, whole structures in spite of their outline. However, due to their distinct non-Gaussian cross section that is itself well resolved by Hi-C 2.1, in this study they are considered to be subsequently modeled as the combination of several Gaussian-shaped coronal strands.

The observed Hi-C 2.1 intensity profile of a cross-sectional slice is reproduced by simultaneously fitting Gaussian profiles, the number of which is determined by the Akaike Information Criterion (AIC; Akaike 1974) along with a corrective term (AICc) for small sample sizes. This is fully described in Appendix. Subsequently, the full width at half maximum (FWHM) of the Gaussian profile is measured to provide an estimate of the possible width of the sub-structures likely present within the Hi-C 2.1 data.

Thus, the method employed to fit Gaussian profiles to the observed Hi-C 2.1 intensity is as follows. First, the following expression for a Gaussian function, Y_G is used:

$$Y_G = A \exp\left(\frac{-(x - x_p)^2}{2W^2}\right), \tag{1}$$

whereby x is the position along the cross-section slice, A and x_p are the amplitude and location of the peak, and W is the Gaussian rms width. This can be related to the FWHM by: FWHM $= 2\sqrt{2\ln 2}\ W \approx 2.35\ W$.

An estimate is made on the number of structures, N that could be present within the intensity profile along with their approximate location, width, and amplitude. Summing the Y_G values for N number of Gaussian curves at each pixel yields the model fit:

$$f(x) = \sum_{i=1}^{N} Y_{G(i)}(x). \tag{2}$$

The closeness of the fit at each pixel, $\chi^2(x)$ is then determined by measuring the deviation of the fit from the original intensity:

$$\chi^2(x) = \left(\frac{f(x) - y(x)}{\sigma(x)}\right)^2, \tag{3}$$

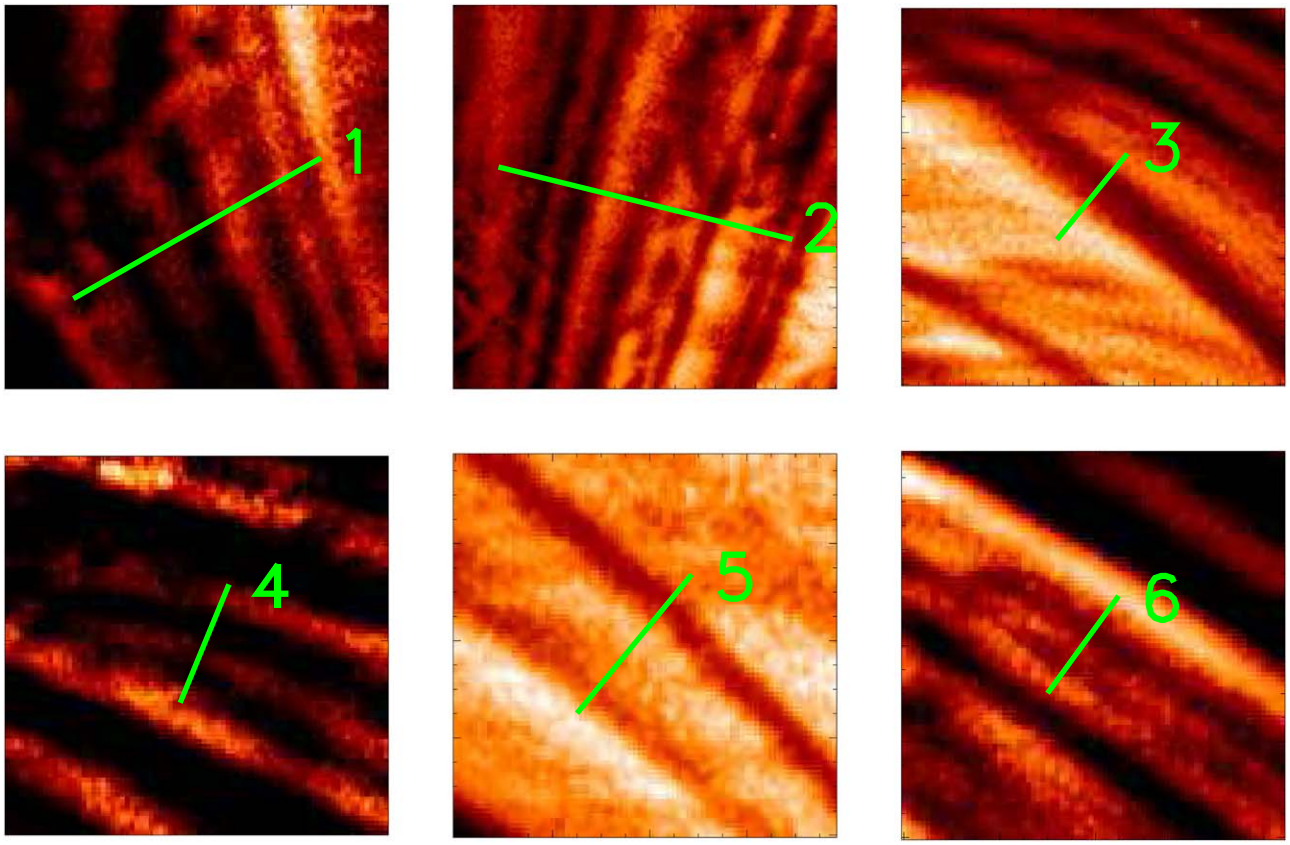

Figure 3. A close-up view of slices numbered 1–6 in Figure 1, which have been sharpened using MGN. The color tables are normalized to each sub-region and are shown in reverse color. The cross-sectional profiles of these slices are shown in Figures 4 and 5.

where $y(x)$ and $\sigma(x)$ are the observed Hi-C 2.1 intensity and Poisson error at each pixel. The overall closeness of fit is then taken as $\sum\chi^2(x)$, which is then reduced to its smallest value by simultaneously adjusting the free parameters A, x_p, and W for the N Gaussian curves in $f(x)$. The minimization of $\sum\chi^2(x)$ is performed by using the nonlinear least-squares curve-fitting method, MPFIT[5] (Markwardt 2009) which is based on the MINPACK-1 FORTRAN library (Moré 1978). During the fitting process the 1σ uncertainties are returned from MPFIT. These error values are only accurate if the shape of the likelihood surface is well approximated by a parabolic function. Whether fitting multiple Gaussian profiles to each slice satisfies this condition or not would require analysis beyond the scope of this study, however, it is likely the 1σ uncertainties do provide a lower-bound of the FWHM errors.

To determine the appropriate number of Gaussian profiles, N within a given slice, the AIC model selection is employed. This is done by first generating several candidate models, where the number of Gaussian curves differs in each model. The nonlinear least-squares curve-fitting method is then employed for each candidate model and finally the AICc is then computed. The model with the smallest AICc value is then selected as the preferred model for that Hi-C 2.1 slice.

Once the number of Gaussian profiles contained within a Hi-C 2.1 slice is determined, the strand width(s) are taken as the Gaussian FWHM value(s). As with previous loop-width studies (Brooks et al. 2013, 2016; Peter et al. 2013; Aschwanden & Peter 2017; Williams et al. 2020) the width measurements are then collated into statistical samples in order to deduce if key structural widths can be extracted from the data.

[5] MPFIT is freely available at: http://purl.com/net/mpfit.

3. Results and Analysis

Employing the nonlinear least-squares curve-fitting method discussed in the previous section, a total of 183 Gaussian profiles are fitted to 24 Hi-C 2.1 cross-sectional slices. As seen in the FOV plot (Figure 1) it is not easy to completely isolate a coronal strand. For example, to the north of slice 5 (Figure 3) there is an increase in intensity due to a crossing of another emitting feature along the integrated line of sight. Care is taken to avoid contamination from such structures, though it is possible that some residual emission may remain in the slices selected. However, the relative intensity of the much brighter strand to the often weaker contaminating emission means that it is removed during background subtraction.

The following subsections compare the 24 cross-sectional slices to those outlined in Williams et al. (2020) as well as examining the frequency distribution of the newly fitted Gaussian profiles.

3.1. FWHM Method Comparison

Here, comparison is made between the resulting strand widths obtained by fitting multiple Gaussian profiles to Hi-C 2.1 structures versus the widths obtained using the previous method (Williams et al. 2020) now with the improved background subtraction discussed in Section 2.1. Two examples are outlined (Figure 4) where a non-Gaussian distribution is seen. For slice

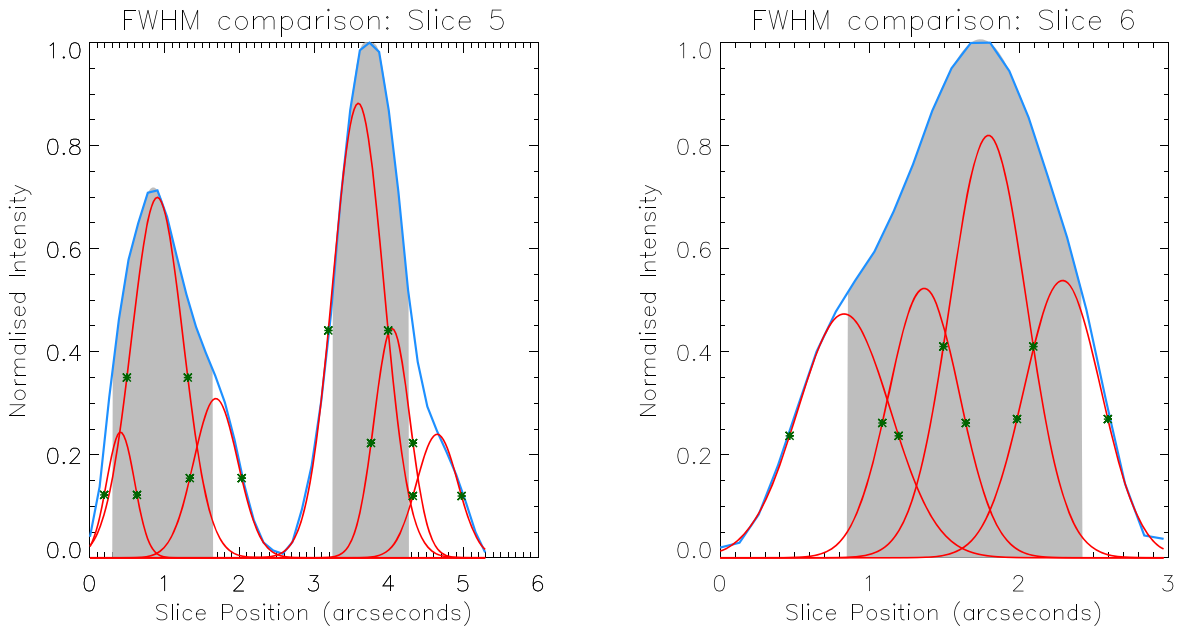

Figure 4. A comparison between the FWHM measurement method of this paper with that of Williams et al. (2020) for slices 5 and 6 shown in Figure 1. The blue line is the background-subtracted Hi-C 2.1 intensity, the Gaussian profiles obtained from using the nonlinear least-squares fitting method are shown in red and their FWHM are denoted by the green asterisks. The solid gray bands indicate the FWHM of the Hi-C 2.1 structures as determined by our previous method (Williams et al. 2020).

5 (6), the AICc determined that six (four) Gaussian profiles are supported by the Hi-C 2.1 data whereas measuring the widths of the non-Gaussian profiles provides two (one) structures.

The Williams et al. (2020) method provides widths of ≈745 and 980 km yielding a mean of ≈860 km for slice 5. Comparatively, the nonlinear least-squares curve-fitting method yields minimum and maximum widths of ≈320 km and ≈590 km, and a mean of ≈480 km. The width of the single structure in slice 6 measured with the Williams et al. (2020) method is ≈1145 km. As with slice 5, the nonlinear least-squares curve-fitting method provides narrower widths with the minimum, maximum, and mean now being ≈405 km, ≈530 km, and ≈450 km, respectively.

The width estimates of the structures centered at 1″ (slice 5) and 10.″4 (slice 6) may be artificially broadened by their shape using the method employed by Williams et al. (2020) due to the observable change in gradient that occurs in the vicinity of the half-maximum intensity value. The structure at 3.″8 (slice 5) does not appear to be affected by this as the change in gradient (or "bump") occurs much lower along the structure than the half-maximum intensity value. However, the measured width of this structure is still ≈300 km broader than the maximum AICc-determined Gaussian width, which indicates previous analysis methods may have over-estimated the strand widths of structures that are potentially not completely isolated from the background and/or other structures along the integrated line of sight.

3.2. Distribution of Fitted Widths

In Figure 5, the cross-sectional profiles (blue) are shown of the Hi-C 2.1 slices numbered 1–4 in Figure 1 along with the best AICc-determined fits and Gaussian profiles generated from the nonlinear least-squares curve-fitting method, shown in red and gray, respectively. From the four examples shown here, it is seen that there is good agreement between the observed Hi-C 2.1 intensity and the generated fit though some minor discrepancies may occasionally occur (e.g., slice 2 between 3.″5 and 6.″5). These discrepancies could be eradicated by adding additional Gaussian profiles along the slices; however, the additional parameters introduced are not supported by the AICc model selection.

In Figure 6(a) the FWHM values of the 183 Gaussian profiles are collated into an occurrence frequency plot binned at 125 km intervals so as to be consistent with the previous study (Williams et al. 2020) where 1″ ≈ 725 km. A sub-section of this data (200–760 km) is shown in Figure 6(b) which is binned at half the spatial scale of Figure 6(a) (62.5 km). Figure 6(c) shows the 1σ errors for the 183 Gaussian widths indicating the majority of errors are $\lesssim$50 km.

The distribution of all analyzed widths in Figure 6(a) reveals that the most populous widths are between 450 and 575 km; this matches the high-emission region results from Williams et al. (2020). The median width for this data is 645 km and is akin to that obtained by Brooks et al. (2013); however, this value is due largely to the presence of a number of broader strands (>1000 km). Furthermore, ≈21% of widths exceed 1000 km while ≈32% of the strands studied are at the SDO/AIA resolving scale of 600–1000 km. From this, ≈47% of the strands are beneath the resolving scale of AIA.

Figure 6(a) reveals the most populous strand widths in this study occur between ≈200 and 760 km with the number of width samples above this spatial scale rapidly decreasing. Figure 6(b) shows a subset of the obtained widths having been re-binned to 62.5 km intervals, which allows for further insight on the distribution of widths for the most populous occurrence frequency bins of Figure 6(a). The obtained Hi-C 2.1 strand widths reveal the presence of numerous strands (≈32% of the 183 Gaussian widths) whose FWHMs are beneath the most frequent high-emission strand widths seen previously (Williams et al. 2020, ≈513 km). Similarly, ≈17% reside beneath an AIA pixel width of 435 km. Comparatively then, only ≈6% of the strands are actually at the the scale at which Hi-C 2.1 can resolve structures (Rachmeler et al. 2019, ≈220–340 km), indicating that current instrumentation may now be beginning to observe a prevalent spatial scale.

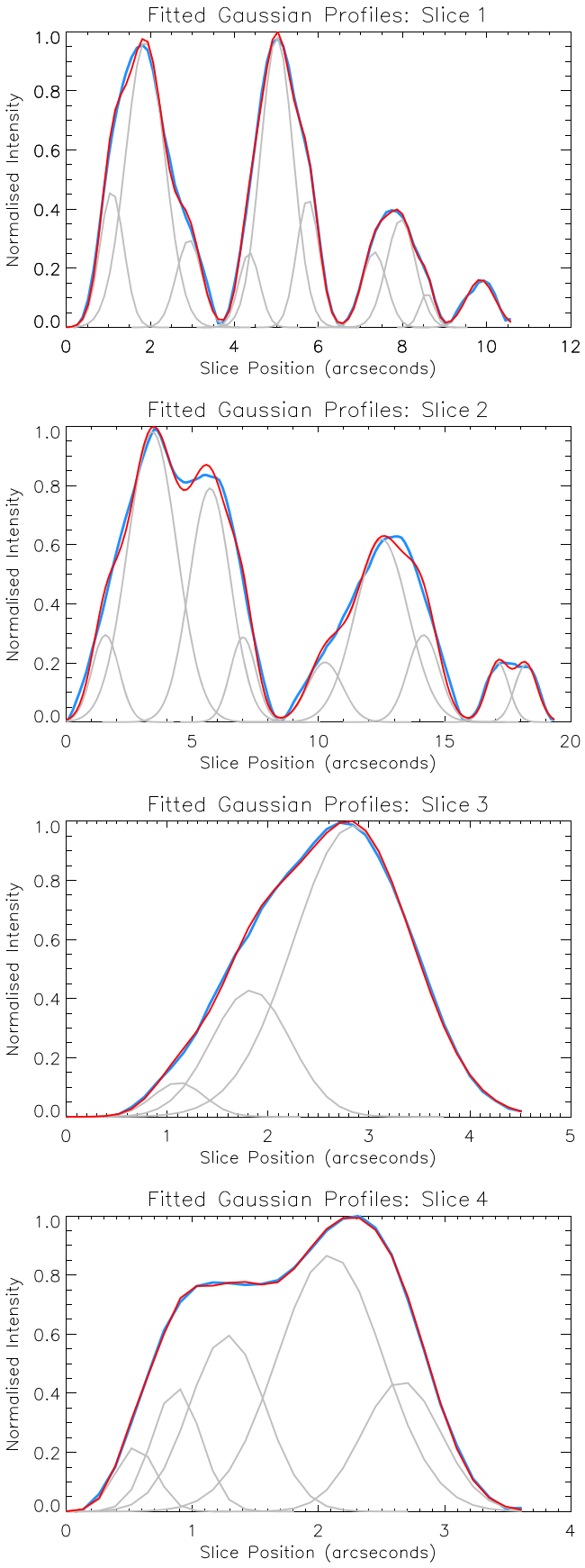

Figure 5. Intensity profiles of the Hi-C 2.1 cross-sectional slices (1–4 in Figure 1) are shown in blue. The Gaussian profiles (gray) generated by the nonlinear least-squares fitting algorithm and the subsequent fit, $f(x)$ (red) are also plotted for the four example slices.

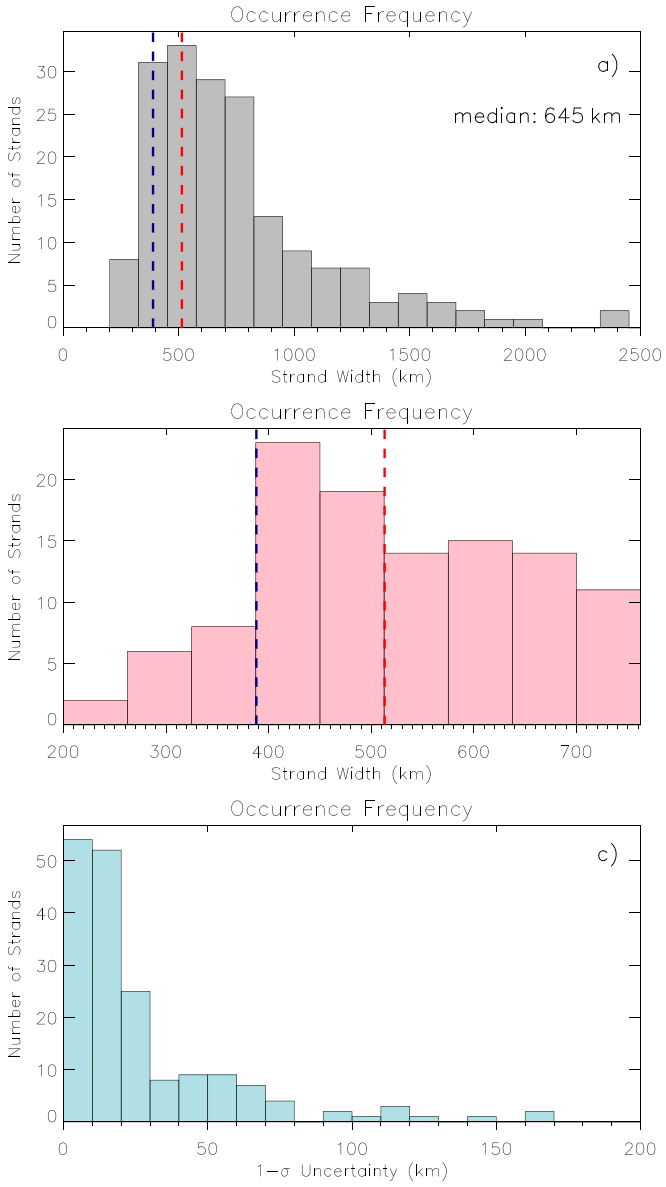

Figure 6. (a) Occurrence frequency plot of the 183 FWHM measurements for the fitted Gaussian curves with a bin width of 125 km; (b) a subset of the Gaussian profiles plotted at bin widths of 62.5 km that correspond to the most populous widths in (a). The dashed vertical navy (red) lines indicate the low (high) emission strand widths obtained in Williams et al. (2020). Panel (c) shows the $1-\sigma$ errors for the 183 widths obtained for the Gaussian profiles in (a).

As with Williams et al. (2020), this analysis reveals that the most-likely strand widths of 450–575 km are typically of the order of an AIA pixel width. This result coupled with the low-percentage (≈6%) of strands at the Hi-C 2.1 resolving scale suggests that the non-Gaussian structures observed are predominately the result of multiple, potentially resolvable strands overlapping along the integrated line of sight rather than the result of finer strands that even Hi-C 2.1 is unable to resolve into distinct features. It should be noted that these results are 50–250 km narrower than previous Hi-C findings that focused on 193 Å emission (Brooks et al. 2013; Aschwanden & Peter 2017).

Nevertheless, this does not rule out the possibility of strands within or beneath the resolving power of Hi-C 2.1. For example, using CRISP Hα data, Scullion et al. (2014) find that the most populous strand width is ≈100 km. However, the

temperature of those structures is 1–2 orders of magnitude lower than that observed with Hi-C 2.1.

4. Summary and Conclusions

This work outlines a follow-up analysis to Williams et al. (2020) where non-Gaussian shaped width profiles that are not fully resolved within the Hi-C 2.1 data are further investigated. To estimate the widths of possible strands, Gaussian functions are first fitted to approximate the Hi-C 2.1 intensity profiles using the method outlined in Section 2.2. The nonlinear least-squares curve-fitting method employed automatically determines the Gaussian rms width due to W being a free parameter (Equation (1)) used to reduce $\sum \chi^2(x)$. The number of Gaussian profiles and subsequently the number of rms widths measured are determined by the AICc, which are then converted to FWHM for our width analysis study.

The FWHM are collated into occurrence frequency plots (Figure 6) revealing the most frequent strand width is ≈450–575 km. The spatial scales obtained in this study largely agree with previous findings (Aschwanden & Peter 2017; Williams et al. 2020) where typical widths the size of an AIA pixel are seen. Additionally, the results reveal that only ≈6% of the strands analyzed reside at the smallest spatial scales that Hi-C 2.1 can resolve into distinct structures (Rachmeler et al. 2019, 220–340 km). Together, these findings strongly suggest that structures emitting at 172 Å that cannot be resolved into distinct features by Hi-C 2.1 are likely to comprise of multiple strands overlapping along the integrated line of sight rather than being an amalgamation of strands at/below the resolving scale of Hi-C 2.1. For coronal loop modeling, the onus must now be on the determination of the spatial scale at which heating occurs that leads to the formation of individual magnetic strands that (i) have widths 450–575 km and (ii) are filled with plasma around 1 MK.

Furthermore, recent work by Klimchuk & DeForest (2020) investigated the widths along the length of isolated coronal structures and found no correlation between width and intensity. However, as is noted in Klimchuk & DeForest (2020), if a structure indicated signs of any possible substructure, then that particular example was not included in the study data. Thus, employing the methods adopted in this work on those rejected examples would allow for that type of analysis to be performed along the observable length of coronal structural sub-elements and not only the aforementioned monolithic features. This will be addressed in a follow-up study using the Hi-C 2.1 dataset examined here.

The highly anticipated ESA mission Solar Orbiter (SolO) will provide close-up (≈0.28 au), high-latitude (34°) solar observations. During the mission there will be several observation windows where the spatial resolution of EUV Imager (EUI) HRI as well as the selected passband (174 Å) will be similar to that of Hi-C. However, it is likely SolO will have longer observation windows over which any target active region may be studied (Hi-C only captures 2.5 minutes of usable data per flight). This will allow for significantly improved strand width determination across many differing coronal structures.

Appendix
Akaike Information Criterion

To determine the number of strands that may be hidden within the Hi-C 2.1 data the Akaike Information Criterion

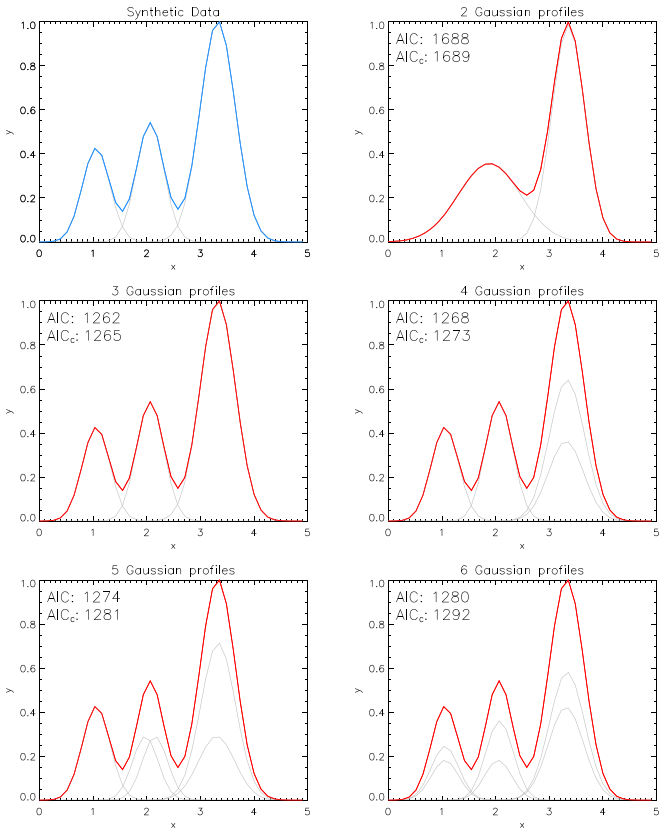

Figure 7. First AIC model selection test case. The upper-left panel labeled synthetic data is generated using three Gaussian functions. Using the Gaussian fitting method employed in this paper, a number of Gaussian functions (shown in gray) are used to replicate the synthetic data and their AIC and AICc values are indicated.

(AIC; Akaike 1974) is employed to determine the optimal number of Gaussian profiles supported by the data. Each additional Gaussian that is added to the model introduces an additional three parameters that may be tweaked to better allow for the observed data to be replicated by Equations (1)–(3). Employing a model selection method such as AIC helps minimize the possibility of selecting a model with too many (few) Gaussian curves, and thus the danger of over(under)-fitting the Hi-C 2.1 data.

Often, the AIC is defined as $\mathrm{AIC} = 2k - 2\ln(L_{\max})$ where k is the number of parameters in the model and $L_{\max}$ is the maximum likelihood. In this study, a least-squares model fitting is employed and thus the maximum likelihood estimate for the variance of a model's distribution of residuals is $\hat{\sigma}^2 = \mathrm{RSS}/n$, where n is the sample size and RSS is the residual sum of squares:

$$\mathrm{RSS} = \Sigma_{i=1}^{n}(y_i - f(x_i))^2. \tag{A1}$$

Thus, the maximum value of a model's likelihood function can be expressed as:

$$-\frac{n}{2}\ln(2\pi) - \frac{n}{2}\ln(\hat{\sigma}^2) - \frac{1}{2\hat{\sigma}^2}\mathrm{RSS} = -\frac{n}{2}\ln\left(\frac{\mathrm{RSS}}{n}\right) + C, \tag{A2}$$

where C is an independent constant that does not change unless y does. Following Burnham & Anderson (2002, p.63), this

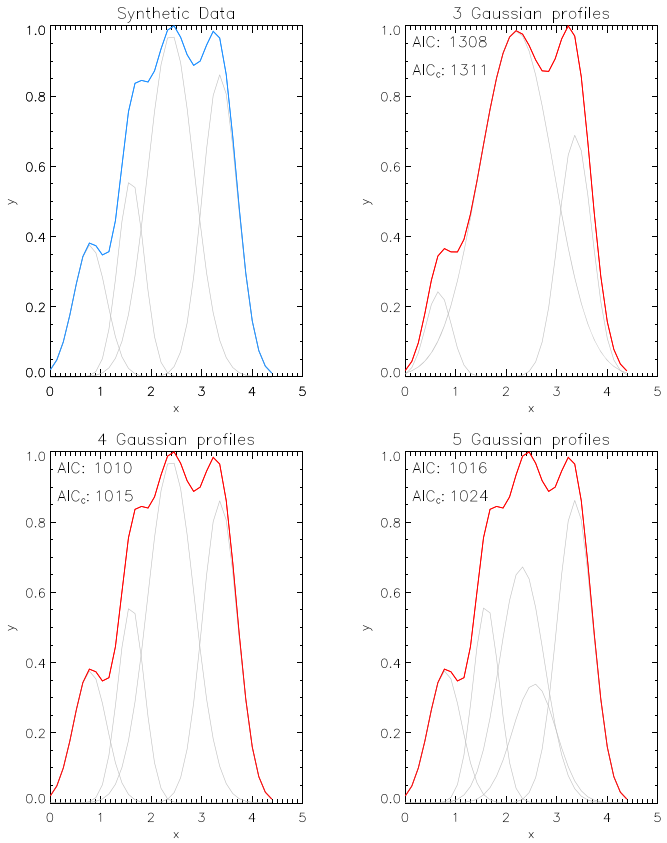

Figure 8. Second AIC model selection test case. The upper-left panel labeled synthetic data is generated using four Gaussian functions. Using the Gaussian fitting method employed in this paper, a number of Gaussian functions (shown in gray) are used to replicate the synthetic data and their AIC and AICc values are indicated.

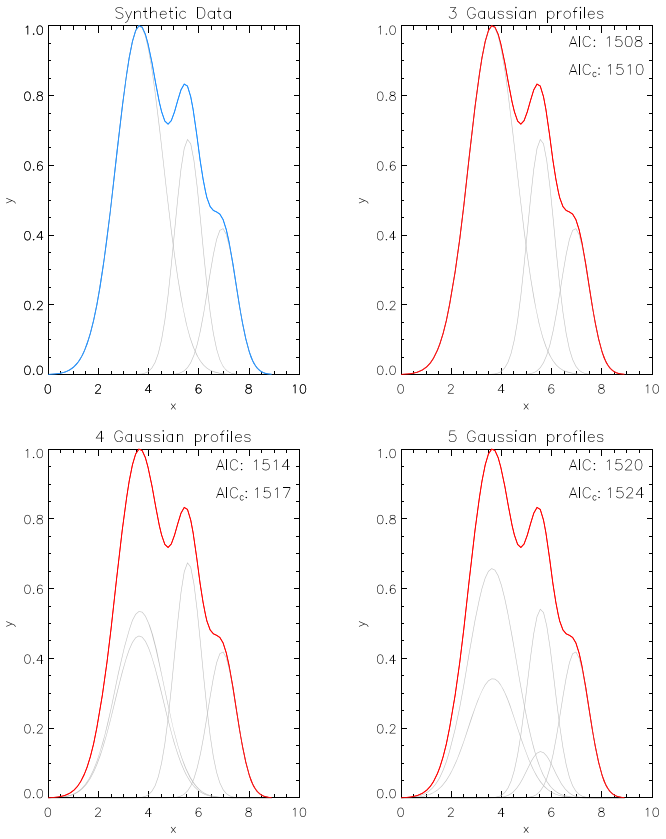

Figure 9. Third AIC model selection test case. The upper-left panel labeled synthetic data is generated using three Gaussian functions. Using the Gaussian fitting method employed in this paper, a number of Gaussian functions (shown in gray) are used to replicate the synthetic data and their AIC and AICc values are indicated.

means the AIC for a least-squares model can be expressed as:

$$\begin{aligned}\mathrm{AIC} &= 2k + n\ln\left(\frac{\mathrm{RSS}}{n}\right) - 2C \\ &= 2k + n\ln(\mathrm{RSS}) - (n\ln(n) + 2C),\end{aligned} \tag{A3}$$

which can be further simplified to

$$\mathrm{AIC} = 2k + n\ln(\mathrm{RSS}), \tag{A4}$$

as $(n\ln(n) + 2C)$ is a constant (provided y does not change) and only the differences in AIC are meaningful.

If n is small, AIC may prefer models which have more parameters and lead to over-fitting of the data. As such, a correction for this is to use the AICc, which provides an additional term accounting for n and k:

$$\mathrm{AICc} = \mathrm{AIC} + \frac{2k^2 + 2k}{n - k - 1}, \tag{A5}$$

that converges to 0 as $n \to \infty$ meaning AICc $\equiv$ AIC for large values of n.

A.1. AIC Test Cases

To validate the AICc model selection, three test cases are devised that are similar to what a Hi-C 2.1 cross-sectional slice may look like in this study. The test cases are generated by specifying a number of Gaussian profiles using Equation (1), which are then combined using Equation (2) to generate the synthetic data for each test case. This process allows for the AICc model selection accuracy to be verified as the number of Gaussian profiles required to generate the three test cases are known.

The first test case is composed of three distinct Gaussian profiles, which is shown by the blue plot in Figure 7. An initial guess on the number of Gaussian profiles (2, 3, 4, 5, and 6 Gaussian curves) and their associated free parameters (A, x_p, and W) are made, which are then passed through our nonlinear least-squares curve-fitting method. During this fitting method, the AIC and AICc values are computed for each model shown in Figure 7. This reveals that the smallest AIC/AICc values are for the model consisting of three Gaussian functions, which matches the number used to generate the synthetic data. Test cases 2 and 3 (Figures 8 and 9) are more complex than the first test case, and subsequently provide a closer representation of Hi-C 2.1 data. Again, the lowest AIC and AICc values correspond to the models consisting of four and three Gaussian profiles, which match the number of Gaussian profiles used in generating the test data.

While both the AIC and AICc show agreement on the model selection for the three test cases analyzed in this appendix, some of the Hi-C 2.1 cross-sectional slices selected may be of sufficiently small sample size that AIC would favor over-fitting the data, which would lead to artificially narrow widths of the strands in question. Therefore and as outlined above, the AICc is employed in this case for determining the number of strands within a given cross-sectional slice.

ORCID iDs

Thomas Williams https://orcid.org/0000-0002-2006-6096
Robert W. Walsh https://orcid.org/0000-0002-1025-9863
Hardi Peter https://orcid.org/0000-0001-9921-0937
Amy R. Winebarger https://orcid.org/0000-0002-5608-531X

References

Akaike, H. 1974, ITAC, 19, 716
Aschwanden, M. J., & Peter, H. 2017, ApJ, 840, 4
Aschwanden, M. J., & Schrijver, C. J. 2011, ApJ, 736, 102
Bray, R. J., Cram, L. E., Durrant, C., & Loughhead, R. E. 1991, Plasma Loops in the Solar Corona (Cambridge: Cambridge Univ. Press)
Brooks, D. H., Reep, J. W., & Warren, H. P. 2016, ApJL, 826, L18
Brooks, D. H., Warren, H. P., Ugarte-Urra, I., & Winebarger, A. R. 2013, ApJL, 772, L19
Burnham, K. P., & Anderson, D. R. 2002, Model Selection and Multimodel Inference: A Practical Information-Theoretic Approach (New York: Springer)
De Pontieu, B., Title, A. M., Lemen, J. R., et al. 2014, SoPh, 289, 2733
Klimchuk, J. A. 2000, SoPh, 193, 53
Klimchuk, J. A. 2015, RSPTA, 373, 20140256
Klimchuk, J. A., & DeForest, C. E. 2020, ApJ, 900, 167
Klimchuk, J. A., Lemen, J. R., Feldmen, U., Tsuneta, S., & Uchida, Y. 1992, PASJ, 44, L181
Kobayashi, K., Cirtain, J., Winebarger, A. R., et al. 2014, SoPh, 289, 4393
Lemen, J. R., Title, A. M., Akin, D. J., et al. 2012, SoPh, 275, 17
López Fuentes, M. C., & Klimchuk, J. A. 2006, ApJ, 639, 459
Markwardt, C. B. 2009, adass XVIII, 411, 251
Moré, J. J. 1978, in The Levenberg–Marquardt Algorithm: Implementation and Theory, Numerical Analysis, ed. G. A. Watson (Berlin: Springer)
Morgan, H., & Druckmüller, M. 2014, SoPh, 289, 2945
Morton, R. J., & McLaughlin, J. A. 2013, A&A, 553, L10
Peter, H., Bingert, S., Klimchuk, J. A., et al. 2013, A&A, 556, A104
Pontin, D. I., Janvier, M., Tiwari, S. K., et al. 2017, ApJ, 837, 108
Rachmeler, A. L., Winebarger, A. R., Savage, A. L., et al. 2019, SoPh, 294, 174
Scullion, E., Rouppe van der Voort, L., Wedemeyer, S., & Antolin, P. 2014, ApJ, 797, 36
Williams, T., Walsh, R. W., Winebarger, A. R., et al. 2020, ApJ, 892, 134
Yi, L., Liu, Z., Wang, K., et al. 2015, NIMPA, 775, 12